Ascending aortic aneurysm in angiotensin II- infused mice: formation, progression and the role of focal dissections

Running title: Ascending aortic aneurysm in Ang II- infused mice

Bram Trachet[1,2], Alessandra Piersigilli[3,4], Rodrigo A. Fraga-Silva[1], Lydia Aslanidou[1], Jessica Sordet-Dessimoz[5], Alberto Astolfo[6], Marco F.M. Stampanoni[6,7], Patrick Segers[2], Nikolaos Stergiopulos[1]

[1] Institute of Bioengineering, Ecole Polytechnique Fédérale de Lausanne, Lausanne, Switzerland

[2] IBiTech - bioMMeda, Ghent University-iMinds Medical IT, Ghent, Belgium

[3] School of Life Sciences, PTEC GE, Ecole Polytechnique Fédérale de Lausanne, Lausanne, Switzerland

[4] Institute of Animal Pathology, Vetsuisse Faculty, University of Bern, Bern, Switzerland

[5] Histology Core Facility, Ecole Polytechnique Fédérale de Lausanne, Lausanne, Switzerland

[6] Swiss Light Source, Paul Scherrer Institut, Villigen, Switzerland

[7] Institute for Biomedical Engineering, University and ETH Zürich, Zürich, Switzerland

Keywords : aortic dissection, aortic aneurysm, ascending aorta, mouse models of human disease, cardiovascular imaging

TOC: basic science, vascular biology

Manuscript: 5962 words, 6 Figures

Supplementary material: 2 Figures, 2 Tables

Bram Trachet

LHTC STI IBI EPFL
BM 5128 Station 17
CH-1015 Lausanne (Switzerland)
Tel: +41 21 693 83 81
bram.trachet@epfl.ch

33

34

35

36

This is a pre-copyedited, author-produced PDF of an article accepted for publication in ATVB following peer review.

39

40

The version of record is available online at:

Ascending aortic aneurysm in angiotensin II infused mice: formation, progression and the role of focal dissections

46

Bram Trachet; Alessandra Piersigilli; Rodrigo A. Fraga-Silva; Lydia Aslanidou, Jessica Sordet-Dessimoz, Alberto Astolfo, Marco FM Stampanoni, Patrick Segers and Nikolaos Stergiopulos

51

52

57

Abstract

Objective. To understand the anatomy and physiology of ascending aortic aneurysms in angiotensin II-infused ApoE$^{-/-}$ mice.

Approach and results. We combined an extensive in vivo imaging protocol (high-frequency ultrasound and contrast-enhanced micro-CT at baseline and after 3, 10, 18 and 28 days of angiotensin II infusion) with synchrotron-based ultra-high resolution ex vivo imaging (phase contrast X-Ray tomographic microscopy) in n=47 angiotensin II-infused mice and 6 controls. Aortic regurgitation increased significantly over time, as did the luminal volume of the ascending aorta. In the samples that were scanned ex vivo we observed one or several focal dissections, with the largest located in the outer convex aspect of the ascending aorta. The volume of the dissections moderately correlated to the volume of the aneurysm as measured in vivo (r^2=0.46). After 3 days of angiotensin II infusion we found an interlaminar hematoma in 7/12 animals, which could be linked to an intimal tear. There was also a significant increase in single laminar ruptures, which may have facilitated a progressive enlargement of the focal dissections over time. At later time points the hematoma was resorbed and the medial and adventitial thickness increased. Fatal transmural dissection occurred in 8/47 mice at an early stage of the disease, before adventita remodeling.

Conclusions. We visualized and quantified the dissections that lead to ascending aortic aneurysms in angiotensin II-infused mice and provided unique insight into the temporal evolution of these lesions.

Abbreviations

AAA: Abdominal aortic aneurysm

TAA: Thoracic aortic aneurysm

PCXTM: Phase Contrast X-ray Tomographic Microscopy

ApoE: Apoliprotein E

2D: two-dimensional

3D: three-dimensional

Micro-CT: micro computed tomography

MMode: Motion mode

BMode: Brightness mode

SR: Sirius Red

Introduction

Aortic aneurysm is clinically defined as a local increase in aortic diameter of at least 50 % compared to the normal diameter[1]. Abdominal aortic aneurysms (AAA) are associated with cardiovascular risk factors such as smoking, age, male gender, hyperlipidemia, hypertension and chronic obstructive pulmonary disease [2]. Although these factors also underlie the majority of thoracic aortic aneurysms (TAA), the latter subgroup incidence is more often related to family history than to the above mentioned factors[3]. Since most aneurysms remain asymptomatic until – often fatal – complications such as rupture occur, our understanding of the pathogenesis, especially in early stages, is limited. Angiotensin II infusion into hypercholesterolemic ApoE$^{-/-}$ mice is a well-known experimental model of both AAAs [4] and TAAs [5]. We have recently explored a novel imaging technique, Phase Contrast X-ray Tomographic Microscopy (PCXTM), to visualize the abdominal lesions of angiotensin II-infused mice [6]. Since the axial resolution of our PCXTM scans (6.5 μm) was close to the thickness of histological coupes for routine morphologic evaluation (4 μm), we introduced PCXTM-guided histology to select sections of the aorta in a highly precise manner for pathology analysis[6]. This approach allowed us to demonstrate that the abdominal lesions in these mice stem from medial ruptures in the suprarenal side branches, leading to media-adventitia dissection with intramural bleeding and thrombus formation [6].

Much like in humans, data on TAAs are scarcer than data on AAAs in mouse models. Daugherty *et al.* reported dilatation of the ascending aorta as semi-quantified on histological sections after 28 days of continuous angiotensin II infusion in ApoE$^{-/-}$ mice [5]. They observed expansion of inter-laminar spaces, collagen deposition and macrophage accumulation. The latter changes were found most extensively within the adventitia while destruction of elastic fibers was observed on the outer convex aspect of the arch. Luminal dilatation [7-9], wall thickening [8, 9] and elastin fragmentation [8, 9] after 28 days of angiotensin II infusion were confirmed by other authors as well. Rateri *et al.* reported a significant increase in diameter of the ascending aorta within 5 days using 2D high-frequency ultrasound. They also reported interlaminar hemorrhage at early time points[9]. Furthermore they consistently observed mural medial breaks within the anterior aspects of the aorta [9]. Although detailed research on morphology, topography and translational aspects of these ascending aorta lesions is still lacking, the mouse model is a common and convenient tool in pre-clinical pharmacological [10-13] and/or gene therapy [14] studies.

In the current manuscript, we combined in vivo imaging with PCXTM and PCXTM-guided histology to visualize, characterize and quantify the lesions in the ascending aorta of angiotensin II-infused ApoE $^{-/-}$ mice. We performed a longitudinal study with sacrifices at different time points, hence stages of disease development. A large number of lesions, particularly those found at the earliest time points, did not qualify as ascending aortic aneurysms from the patho-morphological point of view (not all layers were involved) nor the clinical point of view (no sufficient increase in lumen size). The study of these premature lesions with both established and novel technologies enabled us to present remarkable insights into the pathophysiology and morphology of murine ascending aortic aneurysms over time.

Materials and Methods

Materials and Methods are available in the online-only Data Supplement.

Results

Aortic dimensions and aortic regurgitation

Using the clinical criterion of an increase in aortic size of 50%, 1/22 cases measured with MMode, 3/27 cases measured with BMode and 5/11 cases measured with micro-CT could be diagnosed with an ascending aortic aneurysm (comparing for each technique the aortic size at the latest available time point to the aortic size at baseline, in the animals that were scanned successfully at least twice). The ascending aorta diameter as measured with MMode (1D) increased significantly over time, but a statistically significant difference was only detected between baseline and day 28 (Figure 1e, Table I). The aortic area as measured with longitudinal BMode (2D) and contrast-enhanced micro-CT (3D) increased highly significantly over time ($p<0.001$) and differences were significant in between intermediate time points as well (Figure 1f-g, Table I). Aortic regurgitation as quantified from pulsed Doppler measurements was present but very low at baseline (day 0), and was significantly higher than baseline from day 10 on (Figure 1h, Table I).

Wall strain and thickness

Circumferential Green-Lagrange strain decreased significantly over time ($p<0.001$). A sharp decrease occurred between baseline and day 3, after which the strain values stabilized (Figure 2b, Table I). Both intima-media thickness and adventitial thickness as measured on SR-Miller stains were significantly different between angiotensin II-infused mice and controls (Table I). The medial thickness only reached a significant difference after 28 days (Figure 2c) while the adventitial thickness was already significantly different from saline-infused controls at day 10 (Figure 2d). There was also a trend for increased collagen content in the wall ($p=0.51$, Table I, Figure 2e).

Focal dissections in the ascending aorta

In n=41/42 scanned samples the ex vivo PCXTM images revealed at least 1 and maximum 4 dissections, defined as "gaps" in the aortic wall of at least 10% of the local wall thickness (Figure 3a). The geometric mean of the dissection length was 1.07 mm per sample [95% CI: 0.81 – 1.41], its wall surface area was 0.97 mm² [95% CI: 0.65 – 1.46] and its wall volume was 0.022 mm³ [95% CI: 0.013 – 0.037]. No dissections were observed in control animals. While the largest dissections occurred at the latest time points, no significant difference in lesion volume was observed between the investigated time points of angiotensin II infusion (Figure 3b, Table I). There was a significant difference in dissection incidence and dissection size in between circumferential quadrants. The lowest number of dissections occurred on the inner convex aspect of the aorta, with pairwise comparisons being significant between the inner convex and right aspects (Figure 3c, Table II). The largest dissections occurred on the outer convex quadrant of the aorta, with pairwise comparisons being significant between the outer convex and left quadrants (Figure 3c, Table I). The volume of the ascending aorta as measured with micro-CT prior to sacrifice (Figure 1c - red) correlated moderately ($r^2=0.46$) with the volume of the dissections (Figure 3a - orange, Figure 3d).
The dissections were characterized on image-guided histology by a loss of continuity in at least three adjacent inner elastic laminae of the tunica media (Figure 4a, 4c). Applying the morpho-pathological criterion for an aneurysm (i.e. a vascular outpouch

6

189 involving all layers of the wall [15]) one could state that only 54% of the investigated
190 stains that showed (part of) a dissection had developed a true ascending aortic
191 aneurysm (Figure 4b). Apoptosis of smooth muscle cells was most outspoken at the
192 latest time points and at the edges of the dissection (Figure Ia). The remaining, intact
193 segments of the vessel did not exhibit evidence of ongoing apoptosis.

Interlaminar microhemorrhage

195 H&E stained sections showed that interlaminar microhemorrhages and hematomas
196 occurred after 3 days of angiotensin II infusion (Figure 5a). The hematoma size as
197 measured on HE stains was larger after 3 days of angiotensin II infusion than at
198 subsequent time points, indicating this lesion to be an early step in the pathogenesis
199 of aneurysms in mice (Figure 5c, Table I). The accumulation of extraluminal free
200 erythrocytes occurred more frequently in the outer (abluminal) laminae (L4 – L7); no
201 hematoma was found in the inner two laminae (L1 – L2) (Figure 5d, Table II).
202 Hemosiderophages, stained with Prussian blue, were seen resorbing the hematoma
203 at later time points (Figure Ib). These observations were confirmed on the 3D
204 PCXTM images of the animals that had been scanned with contrast-enhanced micro-
205 CT (Figure 5b). The incidence of extraluminal, intramural Exitron leakage was
206 significantly higher after 3 days of angiotensin II infusion than for controls, but at later
207 time points the difference was no longer significant (Figure 5e, Table I).

Elastic Laminae ruptures

209 The combined SR-Miller stained slides revealed several discrete discontinuities in the
210 medial (elastic) laminae (Figure 6a). Laminar ruptures were present in all animals
211 (Figure 6b, Table II). The total number of laminar ruptures was significantly higher in
212 angiotensin II-infused animals than in controls (Table I). The difference reached
213 significance after 18 days of Ang II infusion (Figure 6b). Neither the incidence nor the
214 number of ruptures varied in between different quadrants (Figure 6c, Table I, II).
215 However, both the incidence and the number of ruptures were significantly different in
216 between layers. The highest number of laminar ruptures occurred in the central
217 laminae (L2 – L4) while the outer laminae (L1, L7) were less frequently affected
218 (Figure 6d, Table I, II).

Transmural dissection

220 All of the 8 animals that were found dead in their cage with hemothorax had died
221 between 3 and 8 days of angiotensin II infusion, during the initial stage of disease
222 development. Six out of these eight ascending aortic samples were scanned ex vivo
223 with PCXTM. In all 6 cases the cause of death could be related to a hemothorax,
224 secondary to the transmural dissection of the ascending aortic wall. PCXTM-guided
225 histology confirmed a complete rupture of all laminae in the tunica media. The
226 transmural dissection ran in the cranial direction (towards the aortic root), be it on the
227 inner convex aspect (Figure IIa) or on the outer convex aspect (Figure IIc) of the
228 aorta.

229

Discussion

In vivo and ex vivo imaging: interpreting the observations

To the best of our knowledge our ex vivo PCXTM images are the first report of volume and location of the focal dissections that cause ascending aortic aneurysms in angiotensin II-infused mice. Despite the focal and asymmetric nature of the wall damage observed ex vivo, an asymmetric outpouch with luminal expansion was not observed in vivo with BMode or micro-CT. Nevertheless the luminal volume observed with micro-CT just prior to sacrifice correlated moderately with the size of the focal dissections observed with PCXTM (r^2= 0.46, Figure 3d). Since the size of the dissections was quantified in the absence of intra-aortic pressure, this correlation does not account for the impact of the dissection on the structural properties and strain of the aorta. Moreover the size of the aneurysm might also be influenced by wall remodeling (Figure 2), intramural hematoma formation (Figure 5) and discrete laminar ruptures (Figure 6), all of which affect the entire wall and not just the region of the dissection. Considering these confounding factors we believe that a correlation of r^2= 0.46 is not insignificant, and that our data support a (possibly indirect) relationship between the size of the observed dissections and the size of the aneurysm in vivo.

Within the different in vivo imaging techniques, the increased accuracy and added information of 2D BMode and especially 3D micro-CT resulted in more overt, more gradual and more significant differences in between different time points than what was obtained with 1D MMode (Figure 1e-g, Table I). Our data thus contradict earlier findings of Rateri et al, who observed a more gradual increase with 1D MMode than with 2D BMode while their BMode measurements reached a plateau value after 7 days of angiotensin II infusion [9]. Moreover 3D imaging enabled us to identify aneurysms that were not picked up by 2D, and 2D imaging was more sensitive than 1D. Since 1D and 2D ultrasound strongly depend on the field of view chosen by the user [16], these findings indicate that for follow-up studies on aneurysm formation 3D images should be acquired when possible.

Both aortic regurgitation and ascending aortic volume were significantly increased after 10 days of angiotensin II infusion (Figure 1g-h). This leads to a dilemma that has also been discussed in a clinical context: did the dilatation of the aorta cause the regurgitation or vice versa? [17, 18]. On the one hand, the fast progression of the disease (both variables were already increased, albeit not significantly, after 3 days) seems to suggest that in angiotensin II-infused mice diastolic regurgitation was the consequence rather than the cause of aortic dilatation, most likely driven by poor leaflet coaptation [19]. On the other hand, once present, diastolic backflow and the subsequent hemodynamic perturbations might have played an important role in the further degeneration of the wall[20]. This is further supported by the fact that the volume of the dissections was larger in the most convex aspect of the aorta (Figure 3c). Aortic regurgitation has been reported to induce aortic remodeling in the outer convex aspect of the ascending aorta in pigs[21]. In human patients with a bicuspid valve, aortic expansion [22] and extracellular matrix protein expression [17] were also increased in the most convex part of the ascending aorta. The latter might thus be a "locus minoris resistentiae" to hemodynamic alterations. Follow-up research is needed to provide more insight into the intriguing role of aortic regurgitation in this mouse model.

Image-guided histology: exploring potential mechanisms

277

278 Since the paraffin cutting (prior to staining) was guided by the PCXTM images, we
279 were able to target the exact region of interest within each analyzed lesion. The
280 analysis of this image-guided histology revealed significant differences between early
281 and late time points of angiotensin II infusion.

282 We observed large intramural hematomas after only 3 days of angiotensin II infusion
283 (Figure 5). The presence of Exitron aggregates within the wall (Exitron is the micro-
284 CT contrast agent that had been injected in vivo) indicates an intra vitam locally
285 increased permeability of the vessel wall, or even loss of continuity of the endothelial
286 lining [6]. In contrast to Rateri et al, who could not identify any access point for the
287 interlaminar hematoma [9], PCXTM (Figure 5b) and PCXTM-guided histology (Figure
288 4a - day 3) allowed us to visualize the intimal defect which led to a mural bleeding at
289 these early time points.

290 We also found an increase in laminar ruptures in the tunica media at an early stage
291 of the disease (Figure 6). Since these laminar ruptures were highly frequent in the 2nd
292 and 3rd lamina (Figure 6d), both of which were affected in all focal dissections (Figure
293 4b), one might hypothesize that the dissections were the result of a progressive tear
294 that had been initiated by a combination of single laminar ruptures. This theory is
295 further supported by the anecdotal observation that 7/41 focal dissections occurred in
296 bilateral pairs, with a tear on the right side of the aorta accompanied by a mirroring
297 one on the left (e.g. Figure 3a, day 10-18 and Figure 4a, day18). If several laminar
298 ruptures culminate into a dissection on one side (left or right) this might locally
299 elongate the aorta and increase the tension on the other side, thus leading to
300 additional laminar ruptures on that side and an ipsilateral, symmetric dissection.
301
302 Since apoptosis was mainly observed at later time points and near the edge of
303 dissections (Figure Ia), it may have played an important role in the progressive
304 enlargement of the lesion over time, rather than being an early event as widely
305 assumed [23]. The progression over time of an initially small tear could also be driven
306 by mechanical forces and factors such as the loss of recoil of adjacent intact elastic
307 laminae, the focal loss of vessel wall compliance (as evidenced by a decrease in
308 circumferential strain, Figure 2b) and interlaminar bleeding (Figure 5).
309
310 After the initial events, further degradation occurred and medial elements were
311 replaced by the deposition of collagen in response to hematoma organization and
312 remodeling of the vessel wall (Figure 2a). Since the medial thickness did not change
313 much after day 10 (Figure 2c) we hypothesize that the formation of granulation tissue
314 (at first) and fibrosis (later on) were counterbalanced by compensatory hypertrophy
315 and/or hyperplasia of the remaining medial smooth muscle cells. This could trigger a
316 vicious circle of degeneration, loss and switch of the contractile phenotype for a
317 secretory one [24]. The altered physical properties of the wall possibly predisposed
318 other sectors of the segment to undergo degenerative medial changes as well.
319
320 We believe that the changes in the adventitia were the result of a combined effect of
321 (i) systemic angiotensin II-induced vessel fibrosis [25] and (ii) local reinforcement of the
322 adventitia near focal dissections, in order to prevent transmural dissection due to the
323 locally weakened tunica media. The latter is further supported by the fact that all fatal
324 transmural dissections occurred after 4.6 ± 1.8 days of angiotensin II infusion (Figure

325 II), when adventitial remodeling was still at a premature stage (Figure 2d-e). A
326 transmural dissection may have occurred in those cases where the focal dissection
327 evolved too abruptly, so that the outer wall segments (which did not have the time to
328 remodel) could not bear the increased load.
329
330 *Translational value of the mouse model*

331 Our previously published PCXTM findings discussed morphological differences
332 between dissecting AAAs in angiotensin II-infused mice and AAAs observed in
333 humans [6]. The focal and partial dissections of the tunica media that we report here
334 have, to the best of our knowledge, never been reported in humans. However, ex
335 vivo images that visualize the entire ascending aortic wall in 3D with a superior
336 resolution are difficult (if not impossible) to obtain in a clinical context. Therefore final
337 conclusions about the translational value of the ascending aneurysms in this mouse
338 model are premature at this stage.
339
340 An important difference between mice and men is the number of laminae in the
341 tunica media (± 7 in mice, ± 50 in humans [26]). Wolinsky and Glagov stated that the
342 tension per lamellar unit is constant (2 N m^{-1}) among species [27], but this was later
343 disputed by Shadwick [28]. Hence the tension on each lamina might be higher in mice.
344 Also, in mice a rupture in one lamina will have a greater impact on the local load-
345 bearing capacity, and the tension on the remaining laminae will be higher. This might
346 explain the observed focal nature of the dissections in mice, and the fast evolution of
347 the disease compared to humans. A detailed computational analysis would be
348 necessary to confirm this hypothesis [29].
349
350 *Limitations and future work*
351
352 In this study baseline measurements (prior to pump implantation) were used as
353 controls for in vivo experiments (ultrasound, micro-CT) while saline-infused ApoE$^{-/-}$
354 mice were used as controls for the ex vivo experiments (PCXTM, histology). We did
355 not investigate the influence of hyperlipidemia on ascending aortic aneurysm
356 formation in this mouse model, and we did not use age-matched controls. These
357 choices were based on the 3R principle (reducing the number of experimental
358 animals as much as possible), and on previous studies reporting negative controls at
359 different time points [8, 9, 13]. Nevertheless, we cannot completely exclude the possibility
360 that the inclusion of normolipidemic mice and/or age-matched controls would have
361 affected the conclusions of our work.

362 We could not find an unequivocal explanation as to why the hematoma was restricted
363 to the outer laminae. We hypothesize that an interstitial outward pressure gradient
364 might be present within the tunica media. Nevertheless, we cannot exclude the
365 possibility that the hematoma was not just caused by an intimal tear, and that
366 additional breaches exist in the outer layers. This theory is supported by the fact that
367 in 3/42 scanned samples a focal hematoma was detected at the level of the aortic
368 arch. Since there was no intimal tear in these cases, these hematomas possibly
369 originated from ruptured vasa vasorum in the outer laminae of the tunica media
370 (Figure IIc).

371   While the largest dissections were found at the latest time point, we did not find a
372   statistically significant increase in dissection size over time. The reason is that a
373   considerable number of animals only suffered from small dissections (Figure 3b)
374   and/or less prominent adventitial remodeling (Figure 2d-e). A similar variability in size
375   and timing of the lesions have previously been observed in dissecting AAAs in this
376   mouse model [30]. This is relatively surprising given the homogeneity of the genetic
377   background in inbred mice and the identical environmental and experimental
378   conditions, and may be related to epigenetic heterogeneity and/or differences in local
379   hemodynamics. Such factors should be taken into account and if possible further
380   elucidated for future studies to empower this model.

381 *Conclusions*

382 We investigated the pathogenesis of ascending aortic aneurysms in angiotensin II-
383 infused mice by longitudinal in vivo monitoring as well as ex vivo synchrotron-based
384 imaging and image-guided histology of the vessel. We visualized how the
385 axisymmetric increase in luminal size that was measured in vivo was related to highly
386 non-symmetric focal dissections within the aneurysm wall, and explored potential
387 disease mechanisms. These novel insights into the morphologic pathology of the
388 aortic wall in ascending aneurysms of angiotensin II-infused mice will help to interpret
389 treatment studies using this mouse model, both prospectively and retrospectively.

390

Acknowledgments

Sources of funding

Disclosures

None.

References

1. Alexander JJ. The pathobiology of aortic aneurysms. *J. Surg. Res.* 2004;117:163-175
2. Sakalihasan N, Limet R, Defawe OD. Abdominal aortic aneurysm. *Lancet.* 2005;365:1577-1589
3. Coady MA, Davies RR, Roberts M, Goldstein LJ, Rogalski MJ, Rizzo JA, Hammond GL, Kopf GS, Elefteriades JA. Familial patterns of thoracic aortic aneurysms. *Arch. Surg.* 1999;134:361-367
4. Daugherty A, Manning MW, Cassis LA. Angiotensin ii promotes atherosclerotic lesions and aneurysms in apolipoprotein e-deficient mice. *J. Clin. Invest.* 2000;105:1605-1612
5. Daugherty A, Rateri DL, Charo IF, Owens AP, Howatt DA, Cassis LA. Angiotensin ii infusion promotes ascending aortic aneurysms: Attenuation by ccr2 deficiency in apoe-/- mice. *Clinical science (London, England : 1979).* 2010;118:681-689
6. Trachet B, Fraga-Silva RA, Piersigilli A, Tedgui A, Sordet-Dessimoz J, Astolfo A, Van der Donckt C, Modregger P, Stampanoni M, Segers P, Stergiopulos N. Dissecting abdominal aortic aneurysm in ang ii-infused mice: Suprarenal branch ruptures and apparent luminal dilatation. *Cardiovasc. Res.* 2015;105:213-222
7. Favreau JT, Nguyen BT, Gao I, Yu P, Tao M, Schneiderman J, Gaudette GR, Ozaki CK. Murine ultrasound imaging for circumferential strain analyses in the angiotensin ii abdominal aortic aneurysm model. *J. Vasc. Surg.* 2012;56:462-469
8. Branchetti E, Poggio P, Sainger R, Shang E, Grau JB, Jackson BM, Lai EK, Parmacek MS, Gorman RC, Gorman JH, Bavaria JE, Ferrari G. Oxidative stress modulates vascular smooth muscle cell phenotype via ctgf in thoracic aortic aneurysm. *Cardiovasc. Res.* 2013;100:316-324
9. Rateri DL, Davis FM, Balakrishnan A, Howatt DA, Moorleghen JJ, O'Connor WN, Charnigo R, Cassis LA, Daugherty A. Angiotensin ii induces region-specific medial disruption during evolution of ascending aortic aneurysms. *Am. J. Pathol.* 2014;184:2586-2595
10. Chen X, Rateri DL, Howatt DA, Balakrishnan A, Moorleghen JJ, Morris AJ, Charnigo R, Cassis LA, Daugherty A. Amlodipine reduces angii-induced aortic aneurysms and atherosclerosis in hypercholesterolemic mice. *PLoS ONE.* 2013;8:e81743
11. Subramanian V, Moorleghen JJ, Balakrishnan A, Howatt DA, Chishti AH, Uchida HA. Calpain-2 compensation promotes angiotensin ii-induced ascending and abdominal aortic aneurysms in calpain-1 deficient mice. *PLoS ONE.* 2013;8:e72214
12. Zhang X, Thatcher SE, Rateri DL, Bruemmer D, Charnigo R, Daugherty A, Cassis LA. Transient exposure of neonatal female mice to testosterone abrogates the sexual dimorphism of abdominal aortic aneurysms. *Circ. Res.* 2012;110:e73-e85
13. Fu X-m, Yamawaki-Ogata A, Oshima H, Ueda Y, Usui A, Narita Y. Intravenous administration of mesenchymal stem cells prevents angiotensin ii-induced aortic aneurysm formation in apolipoprotein e-deficient mouse. *J Transl Med.* 2013;11:175-175
14. Rateri DL, Moorleghen JJ, Balakrishnan A, Owens AP, Howatt DA, Subramanian V, Poduri A, Charnigo R, Cassis LA, Daugherty A. Endothelial cell–specific deficiency of ang ii type 1a receptors attenuates ang ii–induced ascending aortic aneurysms in ldl receptor−/− mice. *Circ. Res.* 2011;108:574-581
15. McGavin MD, Zachary JF. *Pathologic basis of veterinary disease, 4th edition.* Missouri: Mosby Elsevier; 2007.

462   16.   Trachet B, Fraga-Silva RA, Londono FJ, Swillens A, Stergiopulos N, Segers P.
463   Performance comparison of ultrasound-based methods to assess aortic diameter and
464   stiffness in normal and aneurysmal mice. *PLoS ONE*. 2015;10:e0129007

465   17.   Cotrufo M, Corte AD, De Santo LS, Quarto C, De Feo M, Romano G, Amarelli C,
466   Scardone M, Di Meglio F, Guerra G, Scarano M, Vitale S, Castaldo C, Montagnani S.
467   Different patterns of extracellular matrix protein expression in the convexity and the
468   concavity of the dilated aorta with bicuspid aortic valve: Preliminary results. *J Thor
469   Card Surg*. 2005;130:504.e501-504.e509

470   18.   Bissell MM, Hess AT, Biasiolli L, Glaze SJ, Loudon M, Pitcher A, Davis A,
471   Prendergast B, Markl M, Barker AJ, Neubauer S, Myerson SG. Aortic dilation in
472   bicuspid aortic valve disease: Flow pattern is a major contributor and differs with
473   valve fusion type. *Circulation: Cardiovascular Imaging*. 2013;6:499-507

474   19.   Tadros TM, Klein MD, Shapira OM. Ascending aortic dilatation associated with
475   bicuspid aortic valve: Pathophysiology, molecular biology, and clinical implications.
476   *Circulation*. 2009;119:880-890

477   20.   Zhou Y-Q, Zhu S-N, Foster FS, Cybulsky MI, Henkelman RM. Aortic regurgitation
478   dramatically alters the distribution of atherosclerotic lesions and enhances
479   atherogenesis in mice. *Arterioscler. Thromb. Vac. Biol.* 2010;30:1181-1188

480   21.   Atkins S, Cao K, Rajamannan N, Sucosky P. Bicuspid aortic valve hemodynamics
481   induces abnormal medial remodeling in the convexity of porcine ascending aortas.
482   *Biomech Model Mechanobiol*. 2014;13:1209-1225

483   22.   Cotrufo M, Della Corte A. The association of bicuspid aortic valve disease with
484   asymmetric dilatation of the tubular ascending aorta: Identification of a definite
485   syndrome. *Journal of Cardiovascular Medicine*. 2009;10:291-297

486   23.   Durdu S, Deniz GC, Balci D, Zaim C, Dogan A, Can A, Akcali KC, Akar AR.
487   Apoptotic vascular smooth muscle cell depletion via bcl2 family of proteins in human
488   ascending aortic aneurysm and dissection. *Cardiovascular Therapeutics*. 2012;30:308-
489   316

490   24.   Lesauskaite V, Tanganelli P, Sassi C, Neri E, Diciolla F, Ivanoviene L, Epistolato
491   MC, Lalinga AV, Alessandrini C, Spina D. Smooth muscle cells of the media in the
492   dilatative pathology of ascending thoracic aorta: Morphology, immunoreactivity for
493   osteopontin, matrix metalloproteinases, and their inhibitors. *Hum. Pathol.*;32:1003-
494   1011

495   25.   van Thiel BS, van der Pluijm I, te Riet L, Essers J, Danser AHJ. The renin–
496   angiotensin system and its involvement in vascular disease. *Eur. J. Pharmacol.*
497   2015;763, Part A:3-14

498   26.   Abdulkareem N, Smelt J, Jahangiri M. Bicuspid aortic valve aortopathy: Genetics,
499   pathophysiology and medical therapy. *Interactive CardioVascular and Thoracic
500   Surgery*. 2013;17:554-559

501   27.   Wolinsky H, Glagov S. Structural basis for the static mechanical properties of the
502   aortic media. *Circ. Res.* 1964;14:400-413

503   28.   Shadwick RE. Mechanical design in arteries. *J. Exp. Biol.* 1999;202:3305-3313

504   29.   Trachet B, Bols J, Degroote J, Verhegghe B, Stergiopulos N, Vierendeels J, Segers P.
505   An animal-specific fsi model of the abdominal aorta in anesthetized mice *Ann.
506   Biomed. Eng.* 2015;43:1298-1309

507   30.   Trachet B, Fraga-Silva RA, Jacquet P, Stergiopulos N, Segers P. Incidence, mortality
508   and confounding factors for aaa detection in angiotensin ii-infused mice: A meta-
509   analysis. *Cardiovasc. Res.* 2015;108:159-170

510

Significance

Angiotensin II-infused ApoE$^{-/-}$ mice are an important mouse model for aortic aneurysm, but the anatomy of their ascending aneurysms has never been fully understood due to inherent limitations in the currently available small animal imaging technology. In this work we combined in vivo imaging with high-resolution ex vivo imaging and image-guided histology to provide an unprecedented insight into the pathophysiology and the temporal evolution of these lesions. In the short term our aim is to improve the basic knowledge of how ascending aortic aneurysms form in mice, and to serve as a valuable source of insight for past and future studies that rely on this popular mouse model. In the long term we believe that our research will improve future pre-clinical aneurysm research and that it will contribute to enhance our understanding of the initiation of ascending aortic aneurysm in humans.

Figure legends
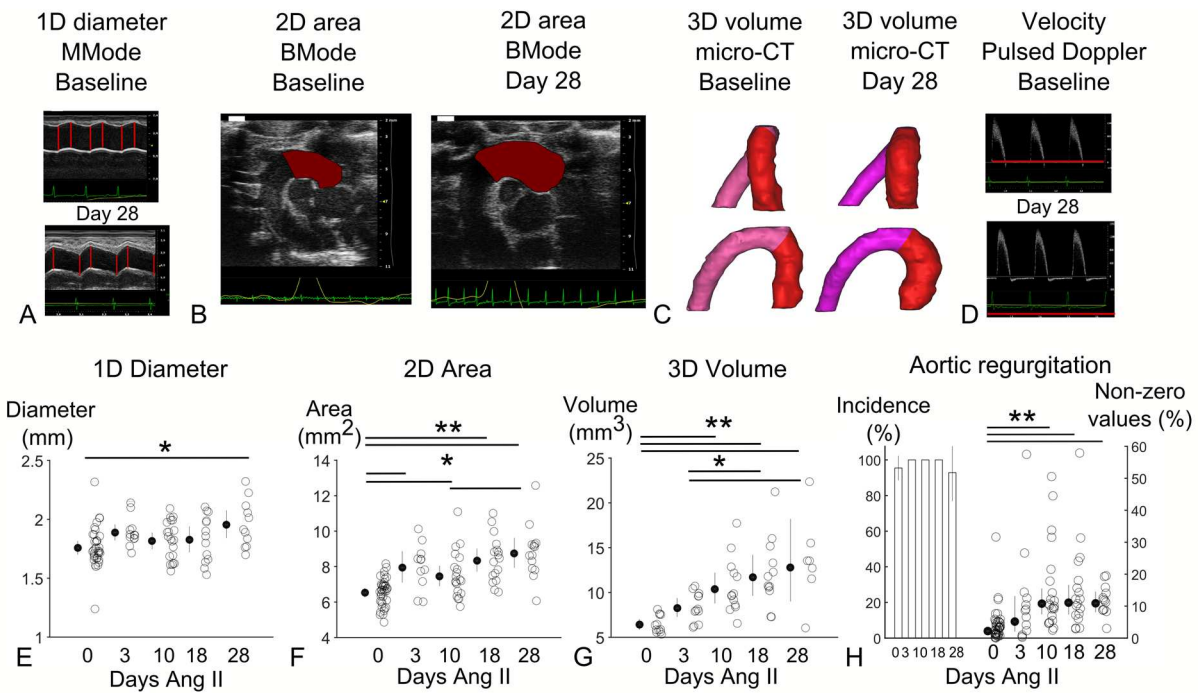
Figure 1. In vivo changes in aortic size and aortic regurgitation severity. Top:
Representative images of in vivo acquisition of size and blood velocity of the ascending aorta
with 1D MMode (**a**), 2D BMode (**b**), 3D micro-CT (**c**) and Pulsed Doppler (**d**). Measured
regions are shown in red. Scale bar represents 1 mm. Scatter plots in panels **e**–**g** show the
measurements at different time points (1D: MMode, 2D: BMode, 3D: micro-CT), as well as
the mean and the 95% confidence interval (calculated in the normal domain after a log
transformation). In panel **h** the bar plots (on the left) show the incidence of aortic
regurgitation for each time point (100*n1/n2, with n1 all mice that have aortic regurgitation at
that time point and n2 all mice measured at that time point) while the scatter plots (on the
right) show the amount of regurgitation in those mice where aortic regurgitation was present
(non-zero values). *: p<0.05, **: p<0.001.
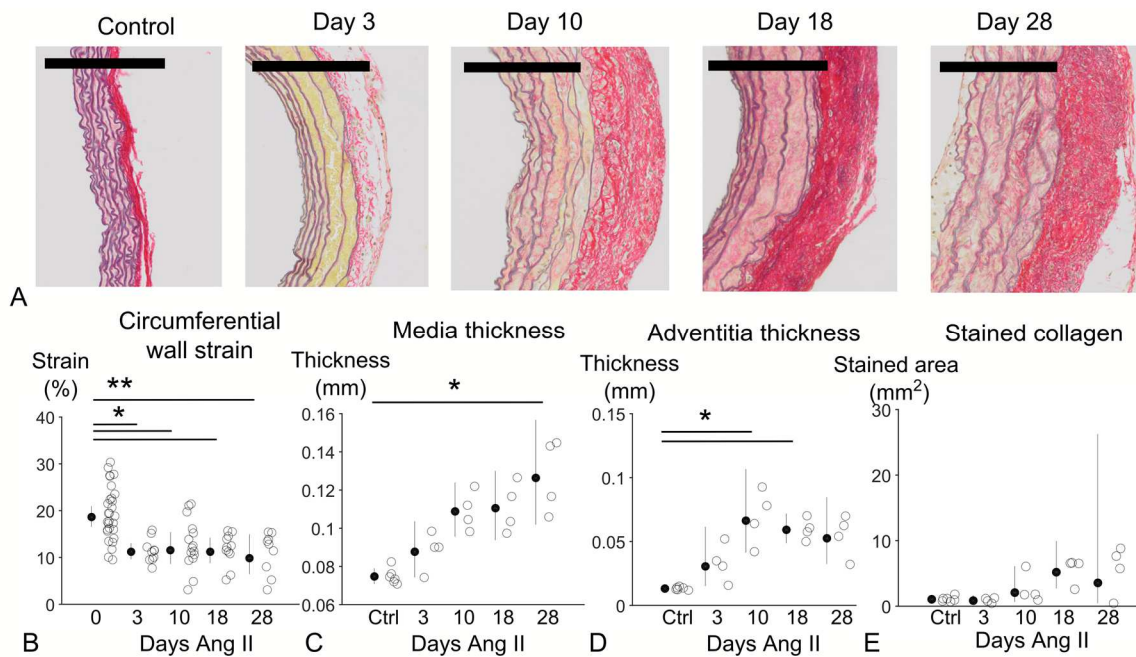
Figure 2. Spatial and temporal variation of aortic wall properties and morphology. Top: Representative Sirius Red – Miller stains showing the aortic wall matrix composition at different time points. Collagen in red, elastin in grey. Scale bar represents 200 µm. Scatter plots in panels **b** – **e** show the evolution of circumferential strain (**b**), intima-media thickness (**c**), adventitia thickness (**d**) and collagen deposition (**e**) over time. The mean and 95% confidence interval are calculated in the normal domain after a log transformation. 3-4 stains, each obtained by image-guided histology,were averaged per animal to account for intra-subject variation. *: $p < 0.05$, **: $p < 0.001$.
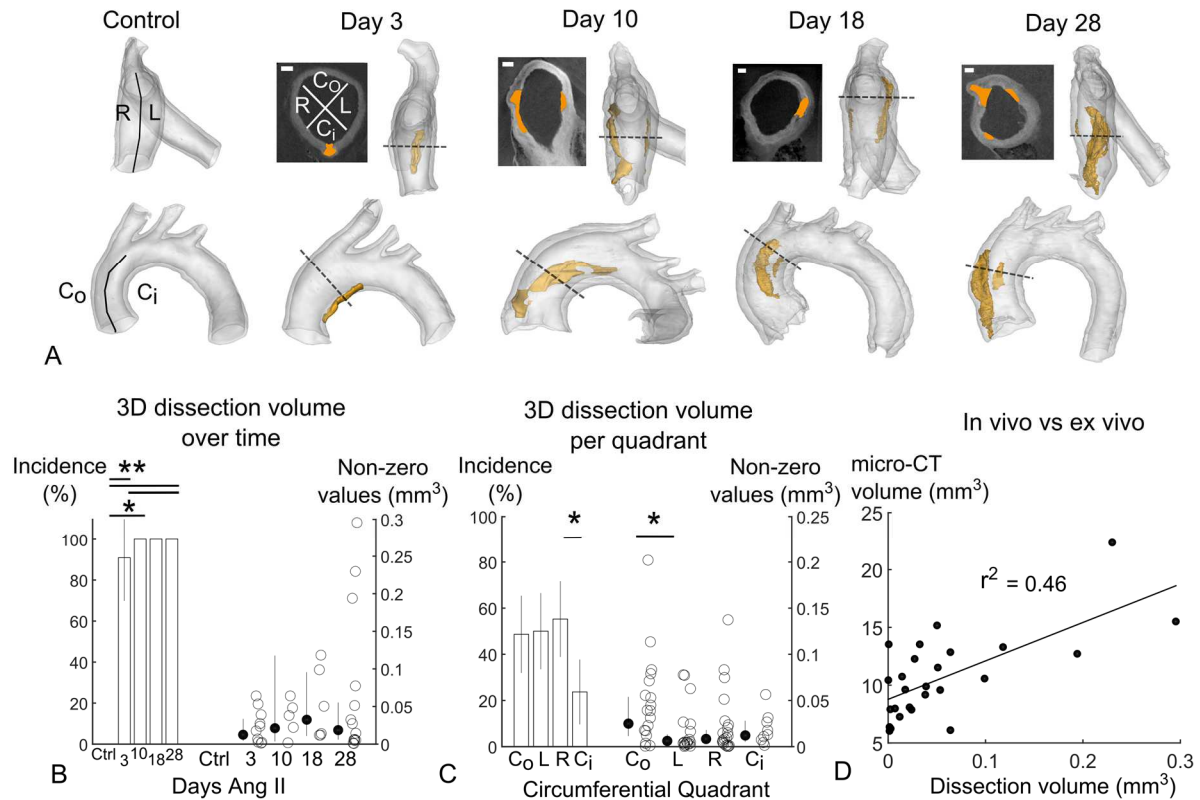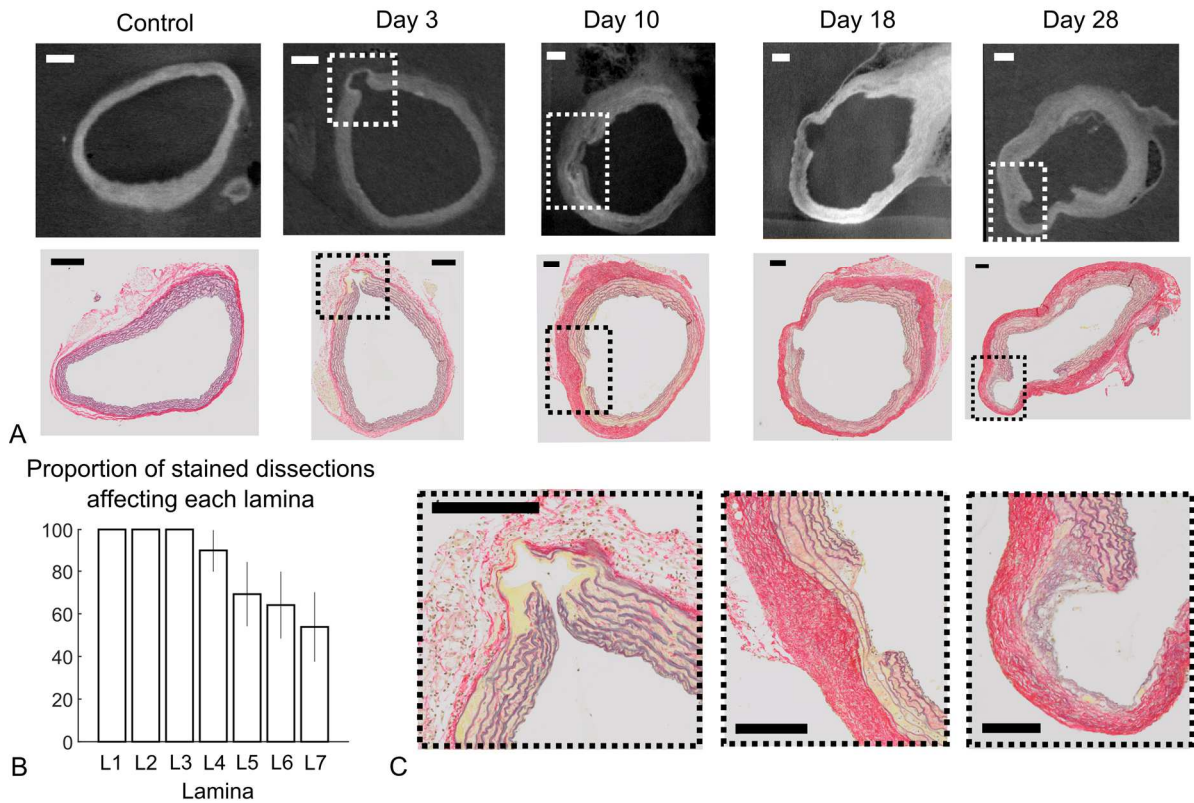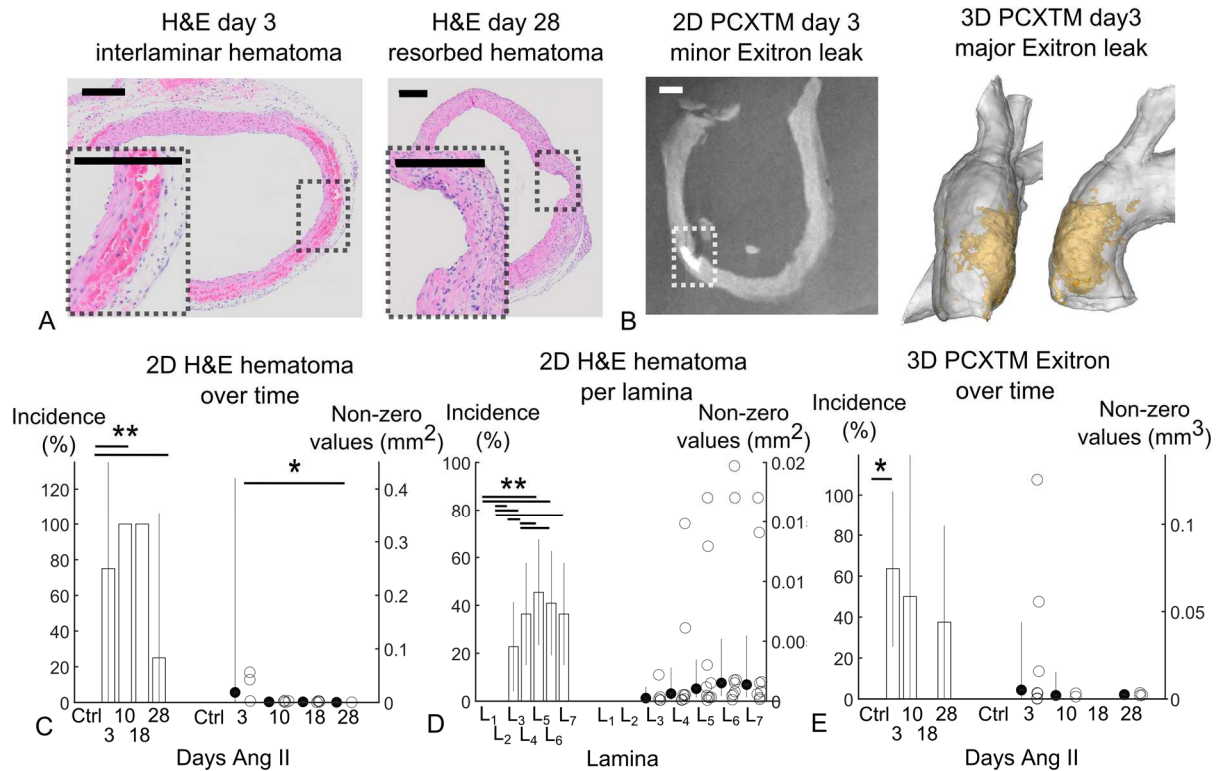
548
549 **Figure 3. 3D PCXTM imaging of focal dissections. a.** 2D and segmented 3D
550 representation of the aortic arch at different time points. Dissections in orange. R: right
551 quadrant, L: left quadrant, C_o: outer convex quadrant, C_i: inner convex quadrant. Scale bar
552 represents 200 μm. **b**. PCXTM-based dissection volume over time. The bar plots (on the left)
553 show the incidence of aortic dissections for each time point (100*n1/n2, with n1 all mice that
554 have a dissection at that time point and n2 all mice measured at that time point) while the
555 scatter plots (on the right) show the volume of the dissections for the non-zero values (n1). **c**.
556 PCXTM-based dissection volume over the circumference. The bar plots (on the left) show
557 the incidence of aortic dissections in each quadrant while the scatter plots (on the right) show
558 the volume of the dissections for the non-zero values. **d.** Scatter plot showing the relation
559 between lumen volume obtained with in vivo micro-CT (Figure 1c, red volume) and
560 dissection volume obtained with ex vivo PCXTM (Figure 3a, orange volume). *: $p < 0.05$, **:
561 $p < 0.001$.

562

Figure 4. 2D PCXTM and SR-Miller stains of focal dissections. a. Top: 2D PCXTM images of focal dissections at different time points. Bottom: PCXTM-guided SR-Miller stains of focal dissections at sections corresponding to the images on top. Scale bar represents 200 μm. **b.** Bar plot indicating the percentage (and 95% confidence interval) of stained dissections in which each lamina was found to be ruptured, relative to the total number of stains in which (part of) a dissection was visible. The total number of stains was obtained across all investigated time points. L1: luminal (intima), L7: abluminal (adjacent to adventitia). **c.** Zoomed sections of (a). Left: a stained dissection in which all laminae (L1-L7) were affected. Right: a stained dissection in which only the inner laminae (L1-L4) were affected.

Figure 5. Spatial and temporal distribution of interlaminar hematoma. a. representative Hematoxin-Eosin (H&E) stains after 3 and 28 days of angiotensin II infusion. Scale bar represents 200 μm. **b.** Left: 2D PCXTM image showing how Exitron (white contrast agent, injected in vivo prior to sacrifice) leaks in between the laminae through an intimal tear. Right: 3D representation of a major Exitron leakage (in orange) that has percolated into the tunica media (in transparent white). **c.** Change in hematoma area over time. The bar plots (on the left) show the incidence of hematoma on the analyzed stains at each time point while the scatter plots (on the right) show the area of the hematoma for non-zero values. **d.** Change in hematoma area per lamina. 3-4 stains, each obtained by image-guided histology, were averaged per animal to account for intra-subject variation. **e.** Exitron volume penetrating into the tunica media over time. *: $p < 0.05$, **: $p < 0.001$.

21
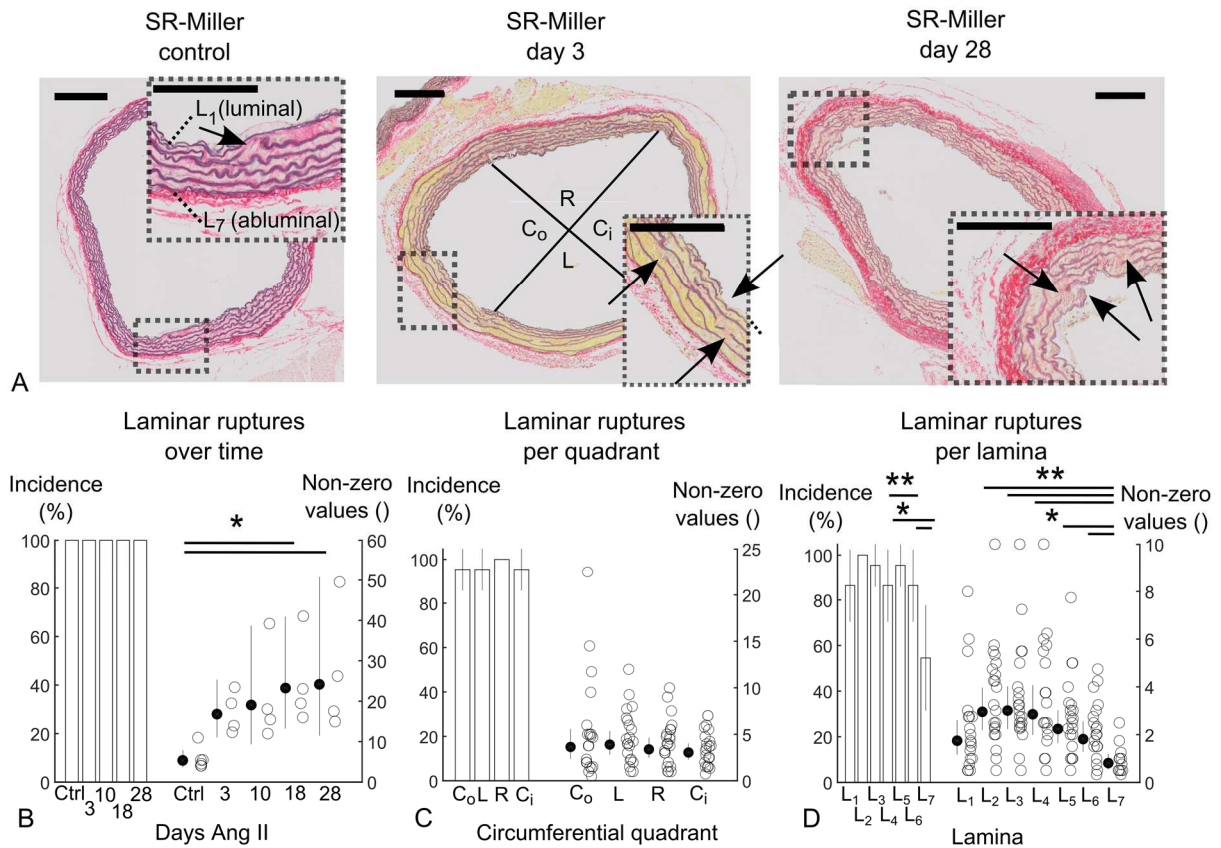
590
591 **Figure 6. Spatial and temporal distribution of laminar ruptures. a**. Representative SR-
592 Miller stains showing elastic laminae ruptures after saline infusion (left) and after 3 (middle)
593 and 28 (right) days of angiotensin II infusion. Laminar ruptures that were part of focal
594 dissections were not taken into account to avoid double reporting. Scale bar represents 200
595 µm. **b.** Laminar ruptures over time. The bar plots (on the left) show the incidence of laminar
596 ruptures at each time point while the scatter plots (on the right) show the number of ruptures
597 for each time point. **c.** Circumferential variation of laminar ruptures. **d.** Change in laminar
598 ruptures per lamina. L1: luminal (intima), L7: abluminal (adjacent to adventitia). 3-4 stains,
599 each obtained by image-guided histology, were averaged per animal to account for intra-
600 subject variation. *: $p < 0.05$, **: $p < 0.001$.

601

Ascending aortic aneurysm in angiotensin II- infused mice: formation, progression and the role of focal dissections

Supplementary Data:

Detailed Materials and Methods

Bram Trachet[1,2], Alessandra Piersigilli[3,4], Rodrigo A. Fraga-Silva[1], Lydia Aslanidou[1], Jessica Sordet-Dessimoz[5], Alberto Astolfo[6], Marco F.M. Stampanoni[6,7], Patrick Segers[2], Nikolaos Stergiopulos[1]

[1] Institute of Bioengineering, Ecole Polytechnique Fédérale de Lausanne, Lausanne, Switzerland

[2] IBiTech - bioMMeda, Ghent University-iMinds Medical IT, Ghent, Belgium

[3] School of Life Sciences, PTEC GE, Ecole Polytechnique Fédérale de Lausanne, Lausanne, Switzerland

[4] Institute of Animal Pathology, Vetsuisse Faculty, University of Bern, Bern, Switzerland

[5] Histology Core Facility, Ecole Polytechnique Fédérale de Lausanne, Lausanne, Switzerland

[6] Swiss Light Source, Paul Scherrer Institut, Villigen, Switzerland

[7] Institute for Biomedical Engineering, University and ETH Zürich, Zürich, Switzerland

Animal model. All the procedures were approved by the Ethical Committee of Canton Vaud, Switzerland (EC 2647.2) and performed according to the guidelines from Directive 2010/63/EU of the European Parliament on the protection of animals used for scientific purposes. Applying the 3R principle (replace, reduce, refine), we used the same animals for a parallel study on abdominal aortic aneurysm formation (yet to be published). The incidence of ascending aneurysms is the same for ApoE [-/-] and regular C57Bl/6J mice[1], while the incidence of abdominal aortic aneurysms is significantly higher for ApoE [-/-] mice[2]. Therefore male ApoE [-/-] mice on a C57Bl/6J background were purchased from Janvier (Saint Berthevin, France). At the age of 12 weeks, n=47 mice were implanted with a 200 µl osmotic pump (model Alzet 2004; Durect Corp, Cupertino, CA), filled with a solution of angiotensin II in saline (Bachem, Bubendorf, Switzerland) as previously described [3]. At the age of 14 weeks, n= 6 control mice were implanted with a 200 µl osmotic pump delivering saline. Each pump infused angiotensin II at 1000 ng/kg/min [4]. Water and regular mouse diet were available *ad libitum* and animals were observed daily after the osmotic pump implantation. Aneurysm onset was instrumentally verified as described later.

Sample size. In total, N= 47 angiotensin II-infused animals and n= 6 controls underwent in vivo imaging. N= 35 out of the 47 angiotensin II-infused animals were included in the long-term in vivo imaging part of the study. N=13 of these animals died with hemothorax (n=7) or hemoabdomen (n=6) during the study. The remaining animals were sacrificed after 10 (n=4), 18 (n=5) and 28 (n=13) days of angiotensin II infusion (Figure 1). These animals were all scanned with ultrasound prior to pump implantation and at each intermediate time point. A subsample (n=11/35) was followed-up with micro-CT at baseline and intermediate time points. Additional micro-CT scans were obtained at intermediate time points if mice from the original micro-CT group died or were sacrificed. This resulted in n=13 micro-CT scans at day10, n=12 at day 18 and n=7 at day 28.

N=12/47 angiotensin II–infused animals were included in the short-term in vivo imaging part of the study. These were sacrificed after 3 days of Ang II infusion. The day 3 animals were all scanned with ultrasound prior to pump implantation and with ultrasound and micro-CT prior to sacrifice. More mice were sacrificed in the short-term study because at this early stage of the disease the differences with controls were expected to be smaller. N=1 animal of this group died with hemothorax after in vivo imaging at day 3, but prior to sacrifice.

In total n=48/53 ascending aortic samples (n=30/33 samples from sacrificed Ang II-infused animals, n=12/14 samples from Ang II-infused animals that succumbed to hemothorax or hemoabdomen, and n=6/6 samples from saline-infused animals) were imaged with PCXTM. Five samples could not be analyzed ex vivo, either because the sample was damaged during dissection (n=3) or because too much time had passed between death from aneurysm rupture and tissue collection (n=2). The operator was blinded during all data analysis.

For ultrasound, micro-CT and PCXTM each animal represents one data point. For image-guided histology a representative, randomized sample of n=4 animals was analyzed at each time point. The goal of image-guided histology was to describe the biological variation within the lesions. If a lesion was visible on PCXTM, image-guided staining targeted 2-3 regions of the lesion in order to capture its start, middle and end. For each animal the final data point represents the mean value of these regions, in order to account for intra-subject variability. If no lesion was visible (e.g. saline-infused controls) 2 regions were analyzed per sample.

In vivo imaging. During both ultrasound and micro-CT imaging, animals were anesthetized with 1.5% isoflurane. Ultrasound imaging was performed with a high-frequency ultrasound device (Vevo 2100, VisualSonics, Toronto, Canada) using a linear array probe (MS 550D, frequency 22-55 MHz). Heart rate and respiration rate were kept constant, and the temperature of the ultrasound table was kept at 40 degrees during the experiment. Blood flow in the ascending aorta was visualized by Color Doppler measurements of the aortic arch and Pulsed Doppler measurements at the level of the ascending aorta (just downstream the aortic valve) and the descending aorta (just distal to the bifurcation of the left subclavian artery). An example of the placement of the Pulsed Doppler probe is shown in Figure Id. Diameter distension waveforms were acquired using radiofrequency (RF) MMode at the ascending aorta, and BMode images of the aortic arch were obtained in longitudinal view. The ultrasound imaging protocol was limited in time for ethical reasons (duration of anesthesia). If measurements did not meet sufficient quality, e.g. due to shadows or reverberations, they were repeated as long as the available time frame permitted so. Images that were still of insufficient quality were excluded from further analysis. Animals followed up in vivo with micro-CT were injected in the lateral tail vein with 4 µl/gram body weight of ExiTron nano 12000 (Miltenyi Biotec, Bergisch Gladbach, Germany) as previously described [5]. After the experiments, mice were anesthetized by Ketamine/Xylazine and the sacrifice was resolved following tissue collection.

PCXTM imaging. After sacrifice, the aorta was flushed in situ by transcardiac perfusion with phosphate buffered saline (PBS, pH 7.4) through the left ventricle. The thoracic aorta was carefully excised and samples were fixated by immersion in freshly prepared 4% paraformaldehyde (PFA) at 4°C temperature for 24 hours. In animals that succumbed to transmural aortic dissection, the aorta was collected (without flushing) as soon as possible after finding them dead. N=48 collected samples were scanned at the TOMCAT beamline of the Swiss Light Source, Paul Scherrer Institut, Villigen, Switzerland. Samples were embedded in 1% agarose gel to stabilize them. The imaging setup consists in two gratings (phase and absorption) with 3.98 and 2 um pitch respectively, positioned at a relative distance of 121 mm. It corresponds to the third fractional Talbot distance at 25 keV. A total of 1441 projections have been acquired over 180 degrees rotations for each of the 5 phase grating steps [5].

Lesion terminology. Throughout the manuscript, a consistent terminology has been used to avoid confusion between different types of lesions that were observed in the aortic wall.
Laminar rupture: a discontinuity of a single elastic aortic lamina (i.e. one of the seven lamellar layers) due to breaks in single lamellar units in the tunica media, as observed on the Miller stain.
Interlaminar hematoma: a local entrapment of free erythrocytes that is confined within the tunica media, between 2 laminae, as observed on the H&E stain.
Dissection (or tear): a discontinuity of the tunica media with a depth of 3 or more consecutive laminae, as observed on the Miller stain. On PCXTM images, dissections were identified as a discontinuity of the tunica media in which the luminal gap corresponds to at least 10% of the wall thickness in an unchanged (normal) area.
Transmural dissection: A full thickness rupture of the aortic wall (including tunica media and tunica adventitia) that leads to hemorrhage and death of the animal by hypovolemic shock.

Image processing. Ultrasound Pulsed Doppler waveforms were traced within a custom-made environment platform in Matlab (Mathworks, Natick, MA) and the average of three different waveforms was computed. The entity of aortic regurgitation in the ascending aorta was subsequently determined as the (dimensionless) ratio of the cumulative integral of negative velocity over the total cumulative integral of positive and negative velocity, both of which were quantified via numerical integration over the flow velocity waveform. A custom-written, Matlab-based application was used to obtain the aortic diameter distension from the 1D RF MMode data. For each diameter measurement, 3 cardiac cycles were selected and plotted as a reference for semi-automatic wall segmentation as previously described [6]. The circumferential cyclic Green-Lagrange strain (eq. 1) was calculated as a measure for aortic compliance under the assumption of uniform strain around the vessel [7].

$$Circ.strain = \frac{1}{2}\left[\left(\frac{D_{sys}}{D_{dia}}\right)^2 - 1\right]*100\% \qquad \text{(eq. 1)}$$

2D Ultrasound BMode images were analyzed using the built-in Vevo tracing software. Area measurements were measured in a longitudinal view, similar to the method proposed by Rateri *et al* [1]. BMode measurements include the ascending aspect of the aorta from (but not including) the aortic valve until (but not including) the branching of the brachiocephalic trunk (Figure 1a, 1b). All reconstructed 3D datasets (in vivo micro-CT as well as PCXTM) were semi-automatically segmented into 3D models using the commercial software package Mimics (Materialise, Leuven, Belgium). Segmentation of the in vivo micro-CT data allowed for quantification of the 3D volume of the pressurized, blood-filled lumen. Volume measurements included the ascending portion of the aorta, just before the branching of the brachiocephalic trunk (Figure 1a, 1b). Segmentation of ex vivo PCXTM data allowed for 3 dimensional quantification of the size of focal dissections. Volume measurements of the dissections quantified the volume of the loss of substance in the tunica media, and thus required extrapolation of the damaged tunica intima (Figure 3a). In order to describe the topography of the circumferential variation of these dissections the ascending aorta was subdivided into 4 quadrants representing the outer convex, left, right and inner convex aspect of the ascending aorta (Figure 3). For each quadrant the total volume of all (parts of) dissections observed in it was computed.

PCXTM-guided histology. After PCXTM scanning, the samples were fixated as mentioned above, processed and embedded in paraffin according to standard histological procedures. 4 µm thick paraffin sections were carefully compared to the corresponding PCXTM images under a Leica DM750 bright field microscope to spot the exact location of dissections. Selected slides were stained with Haematoxylin-Eosin (H&E) to assess general morphology. Miller stain and Sirius red F3B (CI35782, Direct red 80) were combined to specifically highlight elastic fibers and collagen on the same section. Prussian Blue, which is a specific stain for iron, confirmed the cytoplasmic hemoglobin and hemosiderin within macrophages (hemosiderophages) at sites of hematoma resorption. In order to confirm the contribution of smooth muscle cells apoptosis to the progressive degeneration of the media, sections obtained from controls and angiotensin II-infused mice at different time points were co-stained for cleaved caspase 3 and α-SMA on the same slice using the Ventana Discovery XT. Dewaxed and rehydrated paraffin sections were pretreated with heat using the CC1 solution under standard conditions (36 minutes). The primary antibody rabbit anti cleaved caspase-3 (Asp175, Cell Signaling) diluted 1:100 in 1% BSA in PBS was

incubated 1 hour at 37°C. Detection was performed with the secondary rabbit OmniMAp and the DAbMap revelation kit (Roche Diagnostics, Rotkreuz, Switzerland). Antibodies were eluted using heat then the rabbit anti α-SMA (clone E184, Abcam) diluted 1:200 in 1% BSA in PBS was incubated 1 hour at 37°C. After incubation with a donkey α-rabbit biotin antibody diluted 1:500 in 1% BSA in PBS (Jackson ImmunoResearch Laboratories), chromogenic revelation was performed with a BlueMap kit (Roche Diagnostics, Rotkreuz, Switzerland).

Histology image processing. All slides were photographed using an automated slide scanner (VI20-L100, Olympus) and analyzed using a dedicated plug-in in the open source software Fiji [8]. All slides were carefully compared to the stack of 2D PCXTM images as well as the segmented 3D PCXTM vessel in order to determine the orientation of the slide. Each intersection was subsequently subdivided into one of four quadrants. Outer convex, inner convex, left and right aortic quadrants were determined based on the exact match between 2D PCXTM and image-guided histology. Combined thickness of the tunica intima and media as well as thickness of the tunica adventitia were measured on combined SR-Miller stains. In order to account for local variations in thickness, 32 measurements were made for each scanned slide: 4 measurements per quadrant for both the intima-media and the adventitia. Furthermore the number and size (in mm^2) of focal dissections was quantified on SR-Miller stains for each quadrant. Similar to the PCXTM measurements, the size of the lesions was quantified as the area of loss of substance (dissection) in the wall. The number of laminar ruptures was quantified for each elastic layer and for each quadrant on SR-Miller stains. In order to avoid double reporting of data, laminar ruptures that formed part of a focal dissection (i.e. loss of continuity of three consecutive luminal laminae) were not included in the count. Finally, the size of interlaminar hematomas was quantified on Haematoxylin-Eosin (H&E) sections as the area occupied by extraluminal free erythrocytes. This area was computed for each quadrant and outside each lamina. Laminae were ordered from the luminal (L1) to the abluminal (L7) side. If less than 7 laminae were present, no values were counted for L7. If more than 7 laminae were present, results for L8 were added to those of L7. Given the low variation in lamellae in between mice [9], both effects were rare and cancelled each other out. A semi-quantitative measurement of collagen deposition was performed by image analysis (ImageJ). The image was split into its RGB channels and the Green channel was used for image analysis. The aortic wall was segmented manually and the same threshold was used for all analyzed images.

Statistics. For all in vivo experiments the baseline scans (and not the saline-infused control animals) served as control data. All data from in vivo experiments were first transformed from the lognormal to the normal domain by a log transformation. Log-transformed data were tested for normality by the Shapiro-Wilk parametric hypothesis test and visually checked for adherence to the x=y reference line on a normal probability plot. Equal variance was tested with Bartlett's test. The conditions for parametric testing were met for all in vivo variables and therefore their variation in between time points was calculated using a one-way Anova analysis (Table II). Post-hoc pairwise comparisons were performed using a Bonferroni correction. A p-value of 0.05 was considered significant (*), and a p-value of 0.001 was considered highly significant (**).The mean and 95% confidence interval were first calculated in the normal domain and then back-calculated to the original scale. Therefore geometric means and asymmetric confidence intervals are reported in the Figures and Tables.

823   For the ex vivo experiments (PCXTM and histology), 6 saline-infused mice (and not
824   the baseline data, which were not available ex vivo) served as controls. For the ex vivo
825   measurements we reported the incidence (Table II) and the variation of magnitude
826   within non-zero values (Table I) separately.

827   Incidence was defined as $100*n1/n2$, with n1 all mice that have a non-zero value at
828   that time point (or quadrant, or lamina) and n2 all mice that were measured at that time
829   point (or quadrant, or lamina). Incidence rates were reported as bar plots with 95%
830   confidence intervals. The 95% confidence interval was calculated based on a student`s
831   distribution and SEM=sqrt $(p*(1-p)/n)$. For each analyzed variable the variation of the
832   incidence values in between time points, in between quadrants and in between layers
833   was calculated using a chi-square test (Table II). Pairwise comparisons were
834   performed using a Tukey`s HSD multiple comparisons test. A p-value of 0.05 was
835   considered significant (*), and a p-value of 0.001 was considered highly significant (**).

836   The non-zero values from ex vivo experiments (PCXTM and histology) had fewer
837   measurements per time point than the in vivo measurements. There were too few
838   samples per time point to ascertain normality and the Bartlett test showed significant
839   differences in variance between time points, even after log transformation. Therefore
840   in this case a Kruskal-Wallis analysis was performed, followed by a post-hoc Dunn`s
841   test for pairwise comparisons. A p-value of 0.05 was considered significant (*), and a
842   p-value of 0.001 was considered highly significant (**). For the analysis of ex vivo data
843   in between circumferential quadrants and in between laminae the conditions for Anova
844   analysis were met and a similar approach as for in vivo data was followed.

845

846

References

848   1.   Rateri DL, Davis FM, Balakrishnan A, Howatt DA, Moorleghen JJ, O'Connor WN,
849   Charnigo R, Cassis LA, Daugherty A. Angiotensin ii induces region-specific medial
850   disruption during evolution of ascending aortic aneurysms. *Am. J. Pathol.*
851   2014;184:2586-2595
852   2.   Trachet B, Fraga-Silva RA, Jacquet P, Stergiopulos N, Segers P. Incidence, mortality
853   and confounding factors for aaa detection in angiotensin ii-infused mice: A meta-
854   analysis. *Cardiovasc. Res.* 2015;108:159-170
855   3.   Trachet B, Renard M, De Santis G, Staelens S, De Backer J, Antiga L, Loeys B,
856   Segers P. An integrated framework to quantitatively link mouse-specific
857   hemodynamics to aneurysm formation in angiotensin ii-infused apoe -/- mice. *Ann.*
858   *Biomed. Eng.* 2011;39:2430-2444
859   4.   Wang Y, Ait-Oufella H, Herbin O, Bonnin P, Ramkhelawon B, Taleb S, Huang J,
860   Offenstadt G, Combadiere C, Renia L, Johnson JL, Tharaux P-L, Tedgui A, Mallat Z.
861   Tgf-beta activity protects against inflammatory aortic aneurysm progression and
862   complications in angiotensin ii-infused mice. *J. Clin. Invest.* 2010;120:422-432
863   5.   Trachet B, Fraga-Silva RA, Piersigilli A, Tedgui A, Sordet-Dessimoz J, Astolfo A,
864   Van der Donckt C, Modregger P, Stampanoni M, Segers P, Stergiopulos N. Dissecting
865   abdominal aortic aneurysm in ang ii-infused mice: Suprarenal branch ruptures and
866   apparent luminal dilatation. *Cardiovasc. Res.* 2015;105:213-222
867   6.   Trachet B, Fraga-Silva RA, Londono FJ, Swillens A, Stergiopulos N, Segers P.
868   Performance comparison of ultrasound-based methods to assess aortic diameter and
869   stiffness in normal and aneurysmal mice. *PLoS ONE.* 2015;10:e0129007
870   7.   Goergen CJ, Barr KN, Huynh DT, Eastham-Anderson JR, Choi G, Hedehus M,
871   Dalman RL, Connolly AJ, Taylor CA, Tsao PS, Greve JM. In vivo quantification of
872   murine aortic cyclic strain, motion, and curvature: Implications for abdominal aortic
873   aneurysm growth. *J. Magn. Reson. Imaging.* 2010;32:847-858
874   8.   Schindelin J, Arganda-Carreras I, Frise E, Kaynig V, Longair M, Pietzsch T, Preibisch
875   S, Rueden C, Saalfeld S, Schmid B, Tinevez J-Y, White DJ, Hartenstein V, Eliceiri K,
876   Tomancak P, Cardona A. Fiji - an open source platform for biological image analysis.
877   *Nat. Methods.* 2012;9:10.1038/nmeth.2019
878   9.   Goergen CJ, Li H-H, Francke U, Taylor CA. Induced chromosome deletion in a
879   williams-beuren syndrome mouse model causes cardiovascular abnormalities. *J. Vasc.*
880   *Res.* 2011;48:119-129